The Astronomical Journal, 127:1014–1028, 2004 February

THE INITIAL MASS FUNCTION AND STELLAR CONTENT OF NGC 3603

Hwankyung Sung
Department of Astronomy and Space Science, Sejong University, Kunja-dong 98, Kwangjin-gu, Seoul 143-747, Korea; sungh@arcsec.sejong.ac.kr

and

Michael S. Bessell
Research School of Astronomy and Astrophysics, Australian National University, MSO, Cotter Road, Weston, ACT 2611, Australia; bessell@mso.anu.edu.au
Received 2003 August 14; accepted 2003 November 10

ABSTRACT

We present *UBVRI* and Hα photometry of the extremely compact, starburst cluster NGC 3603. Ground-based images, *Hubble Space Telescope* (*HST*) archival data, as well as *Chandra* X-ray data have been used for this study. We present, for the first time, optical color-magnitude diagrams (CMDs) for the stars in the cluster core down to $V = 22$ mag. A well-defined main sequence (MS) as well as low-mass pre–main-sequence (PMS) stars can clearly be seen in the CMDs. This result confirms the finding by Eisenhauer et al. that low-mass stars are forming in the starburst cluster. We also derive an age (1 ± 1 Myr) and distance of the cluster ($V_0 - M_V = 14.2 \pm 0.2$ mag, i.e., $d = 6.9 \pm 0.6$ kpc). The interstellar reddening shows a minimum value [$E(B-V) = 1.25$ mag] at the core ($r \leq 0\farcs2$) and increases rapidly up to $E(B-V) \approx 1.8$ mag or even higher with increasing distance from the center, which suggests the presence of a wind-driven cavity near the cluster center as found by Frogel et al. and Clayton. We also determine the radius of the cluster ($r \approx 2'$) from the surface-density profile of bright stars and X-ray sources. To investigate the initial mass function (IMF) of the cluster, we performed a completeness test for the core region. Using the theoretical mass-luminosity relation of MS as well as PMS stars, we derived the IMF of stars imaged with the *HST*/PC1. The surface density of stars in the core is enormously high and decreases gradually with increasing distance from the center. The slope of the IMF also shows radial variation: fairly flat in the core ($\Gamma = -0.5 \pm 0.1$ at $r \leq 0\farcs1$) and gradually steepening ($\Gamma = -0.8 \pm 0.2$ at $r = 0\farcs1 \sim 0\farcs2$ and $\Gamma = -1.2 \pm 0.2$ at $r > 0\farcs2$ of *HST*/PC1). The stars in the halo region of NGC 3603 (outside of *HST*/PC1) seem to be slightly older (age ≈ 5 Myr) and presumably formed before the stars in the core.

Key words: open clusters and associations: individual (NGC 3603) — stars: luminosity function, mass function

On-line material: machine-readable tables

1. INTRODUCTION

NGC 3603 is an extremely compact young cluster in the Sgr-Car arm. It is the most luminous optically visible H II region in the Galaxy (Nürnberger 2003). It is located beyond the tangential point of the Sgr-Car arm at a distance of about 7 ± 1 kpc (Nürnberger & Stanke 2003). Its core contains many early O-type stars as well as three WN6 stars; NGC 3603 is considered a Galactic clone of the starburst cluster R136 in the LMC (Moffat, Drissen, & Shara 1994). The study of NGC 3603 could therefore be a first step toward an understanding of the nature and stellar content of a starburst cluster. The cluster is so compact that it was previously considered a multiple star (van den Bos 1928). This has made it difficult to study the cluster in detail from classical ground-based telescopes. The construction of large ground-based telescopes, the introduction of new technologies—adaptive optics and active optics—and the availability of space telescopes now make it possible to study the cluster in unprecedented resolution both in the spatial and spectral domain.

The first photometric study of the stars in NGC 3603 was made by Sher (1965) who derived the distance to the cluster of 3.5 kpc, far smaller than the currently accepted value of 7 ± 1 kpc. Later, Moffat (1974, hereafter Mo74) revised the distance to the cluster using *UBV* photoelectric photometry. Van den Bergh (1978) obtained a distance to the cluster of $d \sim 7$ kpc, which is consistent with the kinematical distance. On the other hand, Melnick & Grosbøl (1982) determined a somewhat smaller value. Moffat (1983) studied the stellar content of NGC 3603. He presented spectral types of 13 stars in NGC 3603 and confirmed the WN nature of the central multiple system HD 97950 (Walborn 1973). He also found several low-luminosity early O-type stars, as well as three evolved O-, B-type supergiants, and as a result suggested noncoeval star formation in NGC 3603. Melnick et al. (1989) obtained *UBV* CCD photometry and determined the distance and age of the cluster. They also tried to measure the magnitudes of stars near the center, but their values were strongly affected by crowding.

The structure and kinematics of the interstellar medium around NGC 3603 was also investigated. Balick et al. (1980) studied the structure and kinematics using a pressure-scanned Fabry-Perot interferometer and found a small wind-driven "stellar bubble." Clayton (1986) studied the gas motion of the giant H II region in detail. He found major splitting or asymmetry in Hα with peak-to-peak velocity differences of up to 150 km s^{-1}. He suspected that these large-scale motions were set up before the formation of NGC 3603, possibly by the action of earlier supernovae.

In the 1990s much progress was made in the study of the stellar content of NGC 3603 using data from *HST* and large ground-based telescopes. Moffat et al. (1994) used *HST*/PC1 images to study the stellar content in the core of NGC 3603 and compared it with R136 in 30 Dor. They found that for stars brighter than $M_V = -5.0$, the central densities were very similar, but outside $r \approx 1$ pc the density of massive stars in

NGC 3603 plummets to zero, while in 30 Dor it continues to decrease out to $r \approx 130$ pc. Drissen et al. (1995) obtained spectra of 14 individual luminous stars in NGC 3603 using *HST*/FOS. They resolved the central core of NGC 3603 and confirmed three WN6+abs stars and many early O-type stars. Hofmann et al. (1995) deconvolved the core region of NGC 3603 (HD 97950) from diffraction-limited speckle masking observations and obtained an age (3.2 Myr) and somewhat steep IMF ($\Gamma = -1.59$) for the most massive stars ($m \geq 15\ M_{\odot}$).

Brandner et al. (1997) found a ring nebula and bipolar outflows associated with the B1.5 supergiant Sher 25. From the high-resolution echelle spectra, the northeast nebula shows an enhancement in nitrogen, which suggests that Sher 25 is an evolved post–red supergiant. They also discussed the relation between Sher 25 and NGC 3603 and suggested that the starburst in NGC 3603 might have been triggered by the first generation of massive stars through their interaction with a dense cloud core (see also Drissen et al. 1995; Moffat 1983; Melnick et al. 1989). Brandner et al. (2000) discovered three protoplanetary disk (proplyd)-like objects in NGC 3603 whose spectral characteristics are very similar to those of an ultra compact H II region with electron densities well in excess of 10^4 cm^{-3}. However, Nürnberger & Stanke (2003) could find no mid-infrared counterparts for the proplyd-like objects and concluded that they are smaller scale versions of the neighboring pillars.

Eisenhauer et al. (1998) studied for the first time the low-mass PMS stars in NGC 3603 using near-IR images from the adaptive optics system ADONIS on the 3.6 m telescope at La Silla. Their results suggest that low-mass PMS stars are forming even in a massive, starburst cluster. They also obtained the IMF down to sub–solar-mass stars and derived a somewhat flat IMF [$\Gamma(\equiv d \log \xi / d \log m) = -0.7$]. Later, Brandl et al. (1999) confirmed the existence of low-mass PMS stars in NGC 3603 down to 0.1 $M_{\odot}$ from deep near-IR images obtained with the Very Large Telescope Antu unit. Using deep K_s-band images obtained with the infrared camera ISAAC on Antu, Nürnberger & Petr-Gotzens (2002, hereafter NPG02) determined a radius ($r \sim 150'' \pm 15''$) and studied the K_s-band luminosity function of the cluster. They also found that the slope of the IMF down to $M \approx 0.5\ M_{\odot}$ is consistent with that of a Miller-Scalo–type IMF.

Frogel, Persson, & Aaronson (1977) studied several southern H II regions in the mid-IR. They found 15 mid-IR sources in NGC 3603, including the near-IR point source IRS 9. Later IRS 1 and 2 were found not to be point sources, but instead the head of a bright pillar (IRS 1) or an opaque protrusion (IRS 2) (Nürnberger & Stanke 2003). Recently, Nürnberger & Stanke (2003) studied NGC 3603 in the mid-IR using images obtained with TIMMI2 mounted on the ESO 3.6 m telescope. They found 36 mid-IR point sources, mid-IR emission from the three Wolf-Rayet stars WR 43abc, and a number of faint mid-IR sources with very red ($K-N$) colors. In addition, from the subarcsecond mid-IR image, they found two more point sources around IRS 9, the strongest mid-IR source in NGC 3603. Nürnberger (2003) studied the spectral energy distribution and near- and mid-IR colors of the embedded IR source IRS 9A–C and suggested that they are a sparse association of high-mass protostars.

The aims of this study are to investigate the stellar content in the very center of NGC 3603 and to examine the shape and slope of the IMF. In § 2 we summarize our CCD observations, photometry of the *HST* archival data, as well as the *Chandra* X-ray data used in the X-ray source detection. In § 3 we present photometric diagrams and determine some basic parameters for the cluster. In § 4 we describe the tests we used to determine completeness and the results of those tests, and we derive the IMF and its variation in the cluster core. Discussions of the age of stars in the NGC 3603 halo and the formation history of NGC 3603 are given in § 5. Section 6 is the summary.

2. OBSERVATIONS

2.1. *Optical Photometry*

2.1.1. *SSO Observation*

UBVRI and Hα CCD photometry was acquired on 1997 June 2 at Siding Spring Observatory (SSO) with the 40 inch (1 m) telescope (f/8) and a thinned SITe 2048 $\times$ 2048 CCD (24 μm pixels). The scale was $0\farcs602$ pixel^{-1}, giving $20\farcm5$ on a side. Two sets of exposure times were used in the observations (long: 60 s in *I*, 90 s in *R*, 120 s in *V*, 300 s in *B*, 600 s in *U* and Hα; short: 5 s in *V*, *R*, and *I*, 10 s in *B*, 30 s in *U* and Hα). The seeing was $1\farcs7$ in the 120 s *V* image. A finding chart for the observed area is shown in Figure 1. The regions observed by the *HST* and the *Chandra X-Ray Observatory* are also marked in the figure.

The processing, such as overscan correction, bias subtraction, and flat fielding, were done using the IRAF[1]/CCDRED

[1] IRAF is distributed by the National Optical Astronomy Observatory, which is operated by the Association of Universities for Research in Astronomy, Inc., under cooperative agreement with the National Science Foundation.

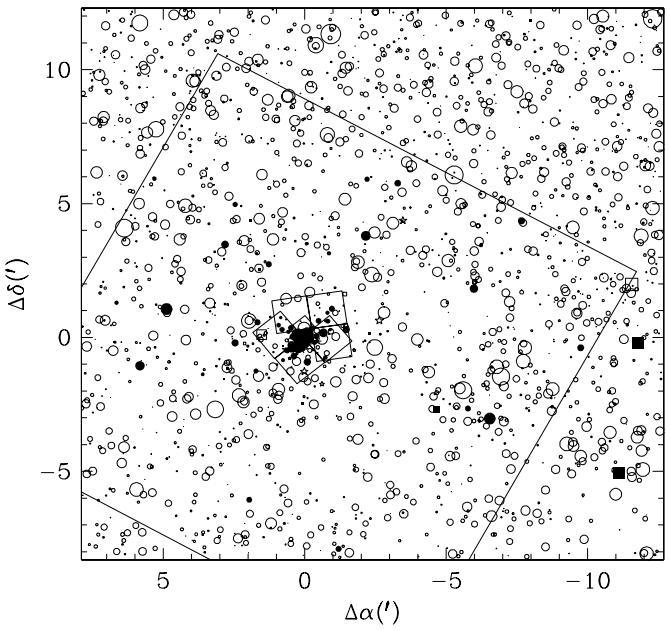

FIG. 1.—Finding chart for stars brighter than $V = 17$ mag based on SSO observations. The size of symbols is proportional to the magnitude of the stars. Open circles represent normal stars, while filled circles, filled squares, open squares, stars, and asterisks represent X-ray sources, Hα-emission stars, Hα-emission candidates, X-ray sources with Hα emission, and X-ray sources with possible Hα emission, respectively. The thick-lined WFPC2 field-of-view (FOV) shows the *HST* region observed using standard filters (F547M, F675W, and F814W), while the thin-lined WFPC2 FOV indicates the region observed with the nebula filters (F656N and F658N). The large square represents the FOV of the *Chandra X-Ray Observatory* ACIS-I.

TABLE 1
COMPARISON WITH PHOTOELECTRIC OR CCD PHOTOMETRY

Author	ΔV	n (n_{ex})[a]	$\Delta(B-V)$	n (n_{ex})	$\Delta(U-B)$	n (n_{ex})	$\Delta(V-I)$	n (n_{ex})
Sher 1965	-0.007 ± 0.062	9 (0)	$+0.009 \pm 0.066$	9 (0)	$+0.026 \pm 0.069$	8 (0)	...	...
Moffat 1974	-0.158 ± 0.107	7 (3)	-0.011 ± 0.039	9 (1)	-0.089 ± 0.057	8 (2)	...	...
van den Bergh 1978	-0.009 ± 0.030	16 (4)	$+0.009 \pm 0.023$	18 (2)	$+0.029 \pm 0.039$	17 (2)	...	...
Melnick et al. 1989	-0.075 ± 0.030	132 (39)	$+0.007 \pm 0.034$	135 (36)	-0.067 ± 0.030	55 (15)	...	...
Pandy et al. 2000	-0.091 ± 0.030	157 (44)	$+0.017 \pm 0.038$	155 (46)	-0.087 ± 0.039	34 (13)	...	...
Sagar et al. 2001	-0.133 ± 0.032	141 (80)	$+0.034 \pm 0.041$	144 (77)	$+0.014 \pm 0.064$	47 (16)	$+0.006 \pm 0.043$	144 (86)

[a] The number of stars used and the number excluded (parenthesized) in the statistics.

package. Instrumental magnitudes were obtained using the IRAF version of DAOPHOT II (Stetson 1990) via point-spread function (PSF) fitting. Finally, the instrumental magnitudes were transformed to the standard Johnson-Cousins *UBVI* system using SAAO E-region standard stars, E5 and E7 (see Sung & Bessell 2000 for details). The mean extinction coefficients ($k_{1U} = 0.533$, $k_{2U} = 0.013$, $k_{1B} = 0.300$, $k_{2B} = 0.031$, $k_{1V} = 0.146$, $k_{1R} = 0.113$, $k_{1I} = 0.082$) were applied because the second half of the night was non-photometric. A total 12,816 stars was measured from the data (photometric data are available from H. S.), but the photometry of the stars in the central region of NGC 3603 is fairly uncertain as a result of the effects of severe crowding.

The *UBVI* magnitude and colors from this study are compared with previous photoelectric or CCD photometry in Table 1. The meaning of Δ is in the sense previous study minus this study. Mo74 and Sagar et al. (2001) show large differences in V, while in $B-V$ all data are well consistent with each other. In $U-B$ the data from three authors (Mo74; Melnick et al. 1989; Pandy et al. 2000) are much bluer than ours, but those from the other three (Sher 1965; van den Bergh 1978; Sagar et al. 2001) are slightly redder within the errors. The large scatter in Mo74 may be caused by errors in the subtraction of the background levels because their stars are located near the cluster center.

2.1.2. *HST Archival Data*

As mentioned above, NGC 3603 is very compact and the photometry from the ground-based images is therefore very uncertain. To investigate the stellar content of the cluster, we retrieved the *HST* archival data. There are two sets of optical images observed in optical passbands. The first set (PI: L. Drissen) was observed in F547M, F675W, and F814W with various exposure times. The other set (PI: E. Grebel) was observed using nebular filters (F656N and F658N) to study the stellar ejecta from the B1.5 supergiant Sher 25.

Both sets of data were reduced using HSTPHOT (Dolphin 2000), which measures the magnitude of stars or extended sources using the model PSF of Tiny Tim.[2] Even though the spatial resolution of *HST* images is much better than that obtained with ground-based telescopes, the effect of many bright stars concentrated in the center is another factor affecting the accuracy and completeness of the photometry. The bright wing and spikes developed around bright saturated images are very important factors affecting the completeness of photometry. From the first pass of the HSTPHOT run, more than 10,000 sources were detected. Many of them were not real stars, but spurious detections of a bright wing or spike. Individual stars were checked on the images. Only very evident starlike point sources were measured again. Finally, magnitudes and colors of 3456 stars (1117 stars in PC1, 892 stars in WF2, 701 stars in WF3, 746 stars in WF4) were obtained. The finding chart for the stars in the *HST*/WFPC2 fields is shown in Figure 2.

The difference ($\Delta \equiv m_{HST} - m_{SSO}$) between our SSO data and the *HST* magnitudes transformed to the ground-based system is shown in Figure 3. In the figure, we only compared stars on the WF chips, because of the effects of crowding on SSO data for the very center of NGC 3603. For $V-I \leq 2.5$, the V magnitudes are very consistent ($\Delta V = +0.016 \pm 0.042$ from 65 stars with $V \leq 18$). In I and $V-I$, the difference is somewhat large [$\Delta I = +0.049 \pm 0.049$ and $\Delta(V-I) = -0.038 \pm 0.039$ from 62 and 66 stars, respectively]. But for $V-I > 2.5$, the differences increase rapidly up to a few tenths of a magnitude. Such a large difference between *HST* data and SSO data for the redder stars may be caused by a large color term for redder stars derived by Holtzman et al. (1995) from synthetic colors. For the convenience of future investigators, we present the data for the 26 brightest stars in the *HST*/PC1 region in Table 2.

We also reduced and analyzed the nebular filter images in an attempt to detect Hα-emission stars near the cluster center. Only two images each were available (500 s $\times$ 2 in Hα and 600 s $\times$ 2 in N [II]), and therefore the photometry is very

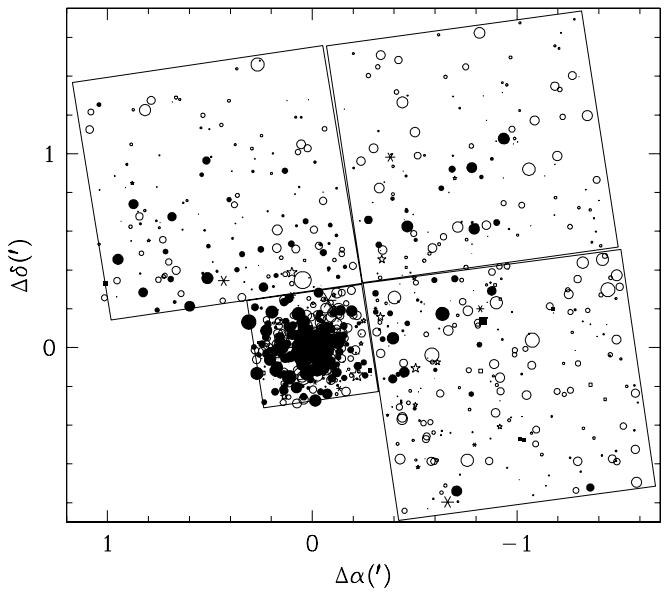

FIG. 2.—Finding chart for stars brighter than $V = 22$ mag based on *HST* data. The thin squares outline the FOV of WFPC2. The other symbols are the same as Fig. 1.

[2] Available at http:// www.stsci.edu/ftp/software/tinytim.

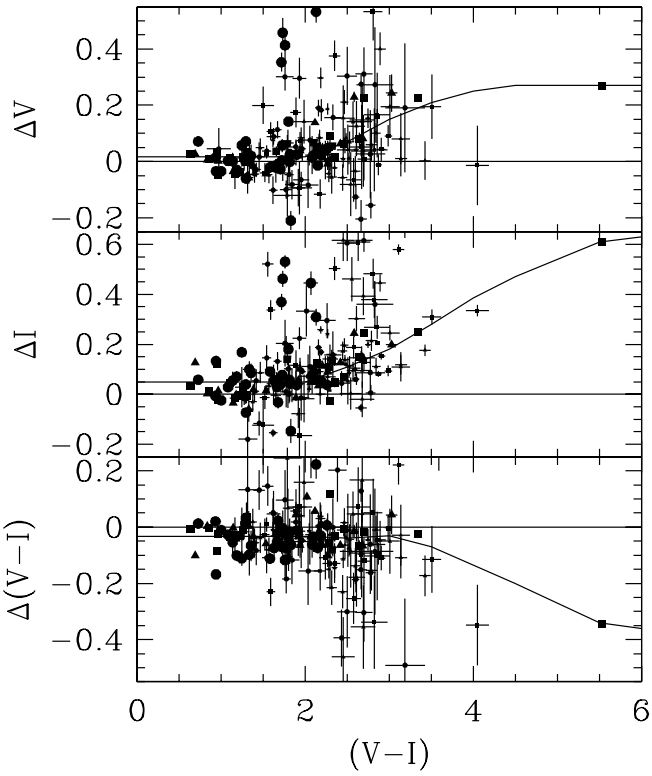

FIG. 3.—Difference between SSO data and *HST* data. The meaning of the Δ is in the sense *HST* magnitude minus SSO magnitude. Circles, triangles and squares represent, respectively, stars in WF2, WF3, and WF4. Large symbols represent bright stars ($V \leq 18$), while small symbols denote faint stars. The thick lines represent the adopted relations to transform *HST* data to SSO data. For $V-I \leq 2.0$, we only applied the mean differences ($\Delta V = +0.016 \pm 0.042$, 65 stars [10 stars excluded]; $\Delta I = +0.049 \pm 0.049$, 62 stars [11 stars excluded]).

limited. The model PSFs for the nebular filters could not be created by HSTPHOT and were kindly made available by A. Dolphin.

2.2. *X-Ray Data*

To select X-ray emission PMS stars in the cluster, we have retrieved X-ray data from the *Chandra X-Ray Observatory* archive (observer ID: 663, PI: M. Corcoran). Using the events file (energy range: 0.3–10 keV) and exposure map, we have run PWDetect, a wavelet-based source detection code for *Chandra* X-ray data (see Damiani et al. 1997 for details) developed at the Osservatorio Astronomico di Palermo. More than 2000 X-ray sources were detected at a significance threshold level above 3.3 σ. Even though the spatial resolution of the *Chandra X-Ray Observatory* is far better than any other X-ray telescopes, the incompleteness of source detection in the central region is very high as a result of the severe crowding.

Optical counterparts of X-ray–emission objects have been identified. For the first pass, we searched for matching optical candidates within an error circle of 3″ from 5 σ detected X-ray sources located at distances $r \geq 2'$ from the center of NGC 3603. We used these identifications to estimate the systematic difference in coordinates between X-ray sources and their optical counterparts. The optical and X-ray positions were in good agreement in right ascension (within 0.″05), but in declination there appeared to be systematic differences that were slightly dependent on the distance from the aim point in declination (1.″14 − 0.″09$\Delta\delta$ [in arcminutes]). After correcting for these systematic differences, we made a more detailed search for optical counterparts of X-ray sources.

Near the cluster center ($r \leq 1'$), the crowding is so severe that it is nearly impossible to identify individual X-ray sources unequivocally. We overlapped the optical sources on the X-ray image and identified the closest star as an X-ray source. For the very center of the cluster, the crowding was too severe to use the original X-ray image. After subtracting the slowly varying background level by employing a median filter technique, we identified the optical counterpart of strong X-ray sources. In this identification process, many weak X-ray sources could be inevitably missed or misidentified because of the effect of crowding. It is worth noting that many faint and bright stars are well matched with X-ray sources, but that moderately bright stars are not. This confirms the suggestion that diffuse X-ray emission near the cluster center could originate from low-mass PMS stars in the cluster (Moffat et al. 2002).

There are two bright X-ray sources outside the NGC 3603 core. The brighter one (significance = 168, $\alpha = 11^{\rm h}14^{\rm m}\ 9\overset{\rm s}{.}5$, $\delta = -61^\circ 14' 33\overset{''}{.}9$) coincides with SB 1104+SB 55976 ("SB" designates the stars in the photometric catalog mentioned in § 2.1). The numbering scheme is described at the bottom of Table 4. This object is an optical double star with $E(B-V) \approx 1.62$ mag and may be an X-ray bright, interacting binary star. The other source (significance = 81, $\alpha = 11^{\rm h}15^{\rm m}21\overset{\rm s}{.}4$, $\delta = -61^\circ 15' 4\overset{''}{.}3$) is coincident with SB 1491 (+SB 57512). SB 57512 is faint and about 3″ away from SB 1491 and therefore may not be related to the X-ray emission. There are 11 X-ray sources with significance better than 10 having no optical counterpart brighter than $V \approx 20$ mag within a 3″ error circle. They are listed in Table 3.

3. PHOTOMETRIC DIAGRAMS

3.1. *Color-Color Diagrams and the Reddening Law*

We present color-color diagrams in Figure 4. In the $U-B$ versus $B-V$ diagram, several groups of stars can be identified. The first is the highly reddened group of hot stars to the right of the reddened zero-age main-sequence (ZAMS) line [$E(B-V) = 1.25$ mag]. They are young stars in and around NGC 3603, i.e., at the far side of the Sgr-Car arm. Many of them are X-ray–emission stars with or without Hα emission (see § 3.3 for the selection of Hα-emission stars). The extension of these stars along the reddening trajectory implies a wide range of reddening among these stars. The second group is also comprised of hot stars, but they are bright and much less reddened. They may be young stars scattered in the general field of the spiral arm. The distance modulus of these stars is about 11 mag (see § 3.4 for details), which is similar to that of NGC 6231 in the Sgr-Car arm (Sung et al. 1998, hereafter SBL98). The third group of stars are late-type field stars in the Sgr-Car arm. The interstellar reddening is similar to that of the second group.

We also present the $B-V$ versus $V-I$ diagram in Figure 4*b*. Most of the field stars in the observed field (the third group) are MS stars in the Sgr-Car arm. Only a small fraction of these stars are reddened giants ($V-I > 2.0$ mag). Young stars in and around NGC 3603 are scattered in the bottom part of the diagram.

To determine the distance to NGC 3603, we need to know the ratio of total to selective extinction, $R_V[\equiv A_V/E(B-V)]$. The R_V-value is related to the color-excess ratio as $R_V = 2.45E(V-I)/E(B-V)$ (Guetter & Vrba 1989). Using 115 bright stars ($V \leq 16.5$ mag and $r \geq 0.'2$ from the center of NGC 3603) with $Q[\equiv (U-B)-0.72(B-V)] \leq -0.5$, we determined

TABLE 2

STARS BRIGHTER THAN V = 14 MAGNITUDES IN THE *HST*/PC1 REGION

ID	R.A. (J2000.0)	Decl. (J2000.0)	V	I	$V-I$	$R-I$	Sp. Type	Remark
1294.....	11 15 08.20	−61 15 47.1	13.305	11.684	1.621	...	...	X
10207.....	11 15 06.23	−61 15 36.1	13.114	11.715	1.399	0.752	O5 V	X
10319.....	11 15 06.58	−61 15 39.9	13.901	12.462	1.439	0.803	...	X?
10361.....	11 15 06.74	−61 15 35.1	13.877	12.464	1.413	0.795	...	X
10363.....	11 15 06.74	−61 15 41.9	13.898	12.475	1.423	0.788	...	X
10392.....	11 15 06.82	−61 15 35.1	12.792	11.315	1.477	0.826	O5.5 III	X
10396.....	11 15 06.84	−61 15 44.2	13.510	11.961	1.549	0.813	O5.5 V	X
10419.....	11 15 06.91	−61 15 36.1	13.261	11.845	1.416	0.774	O3 V	X
10422.....	11 15 06.92	−61 15 38.5	13.053	11.581	1.472	0.823	...	X
10423.....	11 15 06.92	−61 15 38.7	13.248	11.784	1.464	0.780	...	X
10478.....	11 15 07.06	−61 15 38.8	13.017	11.536	1.481	0.804	O3 III(f)	X
10498.....	11 15 07.12	−61 15 38.6	13.391	11.870	1.521	0.821	O3 V	X
10534.....	11 15 07.24	−61 15 36.6	13.507	12.049	1.458	0.846	...	x
10543.....	11 15 07.27	−61 15 34.5	13.081	11.576	1.505	0.797	O3 V	X
10558.....	11 15 07.30	−61 15 38.0	11.629	10.074	1.555	0.804	WN6+abs	X
10559.....	11 15 07.30	−61 15 38.3	12.542	11.046	1.496	0.801	O3 V	X
10570.....	11 15 07.35	−61 15 38.0	13.134	11.629	1.505	0.855	O3 III(f*)	X
10571.....	11 15 07.35	−61 15 39.0	13.789	12.176	1.613	0.870	O5 V+OB	X
10582.....	11 15 07.40	−61 15 38.1	11.121	9.615	1.506	1.017	WN6+abs	X
10616.....	11 15 07.49	−61 15 45.9	13.558	12.017	1.541	0.816	O4V(f)	X
10635.....	11 15 07.59	−61 15 37.6	11.843	10.285	1.558	0.834	WN6+abs	Hα+X
10683.....	11 15 07.75	−61 15 34.7	13.966	12.481	1.485	0.828	O5 V	X
10705.....	11 15 07.82	−61 15 27.5	13.650	12.127	1.523	0.807	...	X
10706.....	11 15 07.82	−61 15 37.4	13.583	12.059	1.524	0.830	O3 V	X
10895.....	11 15 08.51	−61 15 37.8	13.744	12.268	1.476	0.826	...	X
11115.....	11 15 09.84	−61 15 30.0	12.723	11.101	1.622	0.858	O9.5 Iab	X

NOTE.—Units of right ascension are hours, minutes, and seconds, and units of declination are degrees, arcminutes, and arcseconds.

the color-excess ratio (see Fig. 5). The slope is 1.45 ($\pm$ 0.05, s.d.), which is somewhat larger than the normal value (1.25). The R_V-value of this region is 3.55 ± 0.12, which is slightly higher than that of NGC 6231 (SBL98). Because of a lack of reliable $U-B$ and $B-V$ data for the stars in the center of NGC 3603, it is impossible to determine the R_V-value at the cluster center. It may be expected that the ratio is higher there because strong stellar winds could sweep away the small-sized grains near the center. Pandy et al. (2000) also mentioned an abnormal reddening law, but they used instrumental colors.

Figure 5*b* shows the radial variation of interstellar reddening $E(B-V)$. It increases rapidly out to $r \approx 0\farcm2$, reaching about 1.8 mag. The reddening of the cluster center [$E(B-V) = 1.25$] is estimated from the best-fitting ZAMS to the CMD in Figure 7. This result implies that there is a cavity about the cluster center probably due to strong stellar winds (Frogel et al. 1977; Clayton 1986).

3.2. *Color-Magnitude Diagrams*

We plotted several CMDs from ground-based photometry in Figure 6. The reddened ZAMS lines are also plotted (see below for reddening of NGC 3603, and see § 3.4 for distance). The adopted ZAMS relation is discussed in Sung & Bessell (1999). The CMDs in Figure 6 do not show any definite sequence of stars in the cluster. Only a dozen or so X-ray sources constitute a sequence to the right of the reddened ZAMS. In Figure 6*c* one can also see a group of stars well above the ZAMS line. The lack of fainter stars in the sequence is solely due to the extreme

TABLE 3

X-RAY SOURCES WITHOUT OPTICAL COUNTERPARTS BRIGHTER THAN $V \approx 20$ MAGNITUDES

ID	R.A. (J2000.0)	Decl. (J2000.0)	Significance	Count Rate (count s^{-1})
1.....	11 14 01.21	−61 19 01.5	13.57	$1.34\ (\pm 0.21) \times 10^{-3}$
2.....	11 14 03.76	−61 19 10.9	10.54	$1.04\ (\pm 0.20) \times 10^{-3}$
3.....	11 14 27.02	−61 16 22.8	13.59	$7.76\ (\pm 1.40) \times 10^{-4}$
4.....	11 14 37.28	−61 13 09.9	12.37	$7.21\ (\pm 2.04) \times 10^{-4}$
5.....	11 15 02.01	−61 13 24.9	10.44	$4.65\ (\pm 1.43) \times 10^{-4}$
6.....	11 15 04.75	−61 13 57.7	12.35	$6.33\ (\pm 1.81) \times 10^{-4}$
7.....	11 15 07.78	−61 09 54.5	12.82	$1.02\ (\pm 0.02) \times 10^{-3}$
8.....	11 15 12.35	−61 16 55.7	11.45	$5.71\ (\pm 1.63) \times 10^{-4}$
9.....	11 15 15.29	−61 17 01.9	40.01	$4.86\ (\pm 0.33) \times 10^{-3}$
10.....	11 15 15.92	−61 18 03.1	12.07	$5.84\ (\pm 1.67) \times 10^{-4}$
11.....	11 15 22.72	−61 16 12.3	12.15	$5.82\ (\pm 1.15) \times 10^{-4}$

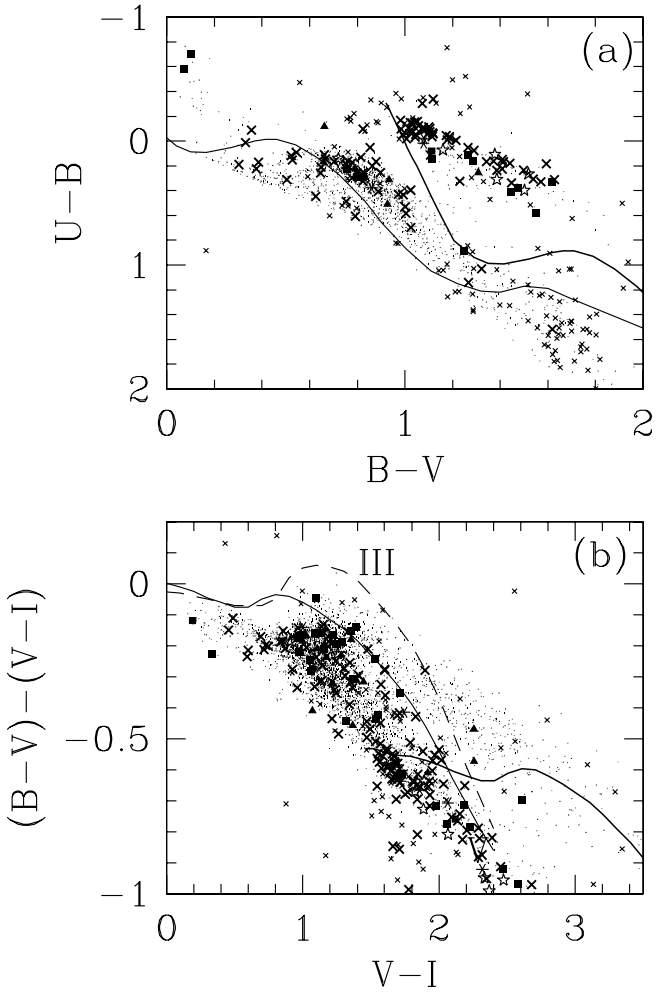

FIG. 4.—Color-color diagrams. (*a*) $U-B$ vs. $B-V$ diagram for $V \leq 17$ mag. The thin and thick lines represent the intrinsic ZAMS relation and the reddened ZAMS relation [$E(B-V) = 1.25$ mag], respectively. (*b*) $B-V$ vs. $V-I$ diagram for $V \leq 18$ mag. The thin dashed line indicates the intrinsic relation for giants. The other two lines are the same as (*a*). In both (*a*) and (*b*) the large cross, square, star, and asterisk represents, respectively, an X-ray–emission star, an Hα-emission star, an X-ray–emission star with Hα emission, and an X-ray–emission star with possible Hα emission. A small dot and small cross denote a star with good photometry ($\epsilon \leq 0.1$) and bad quality ($\epsilon > 0.1$), respectively.

crowding in the cluster core. Normally, Hα photometry is very useful for the detection of Hα-emitting PMS stars (classical T Tauri stars) in young open clusters (see Sung et al. 1997). But in the field of NGC 3603 Hα photometry could not give any definite information on the membership of the cluster. Most Hα-emission stars are not concentrated toward NGC 3603, and so many are probably young stars scattered across the general field of the Sgr-Car arm.

We also present several CMDs from *HST* images in Figure 7. The empirical ZAMS (Sung and Bessell 1999; *thin solid line*) and theoretical ZAMS (Schaller et al. 1992; *thick solid line*, with masses to the left) reddened by $E(B-V) = 1.25$ mag are plotted in the figure. In the transformation of physical parameters to observed quantities we used the synthetic color of Bessell et al. (1998). The PMS evolutionary tracks Siess et al. (2000, hereafter SDF00) are also plotted with masses to the right.

Amazingly, the CMDs from the *HST*/PC1 chip show a well-defined sequence of MS stars, as well as low-mass PMS stars to the right of the reddened ZAMS line. As we know, this is the first optical CMDs to show the existence of low-mass PMS stars in NGC 3603. The spread across the reddened ZAMS line is very shallow [$\Delta(V-I) \approx 0.2$ mag] implying that the amount of differential reddening across the PC1 region is very small [$\Delta E(B-V) \leq 0.15$ mag], which again supports the existence of a cavity blown out by strong stellar winds. Most faint stars in the region coincide with the local bright point in the X-ray image, strongly supporting the proposal that these stars are bona fide low-mass PMS stars in the cluster. Stars fainter than $V \approx 15.5$ mag show a spread to the right of the reddened ZAMS. Some of these stars are located in the outer region ($r > 0.'2$), and so the scatter probably results from differential reddening not photometric errors. For example, star SB 1190 (= 10053, $V = 15.965$, $B-V = 1.368$, $U-B = 0.310$) is a reddened massive star in the peripheral region of PC1.

In § 3.1 we determined the reddening law of the NGC 3603 region. But for the R data from SSO observations we could not transform to the standard system and so could not determine the color excess ratio $E(R-I)/E(B-V)$ directly. We tried to

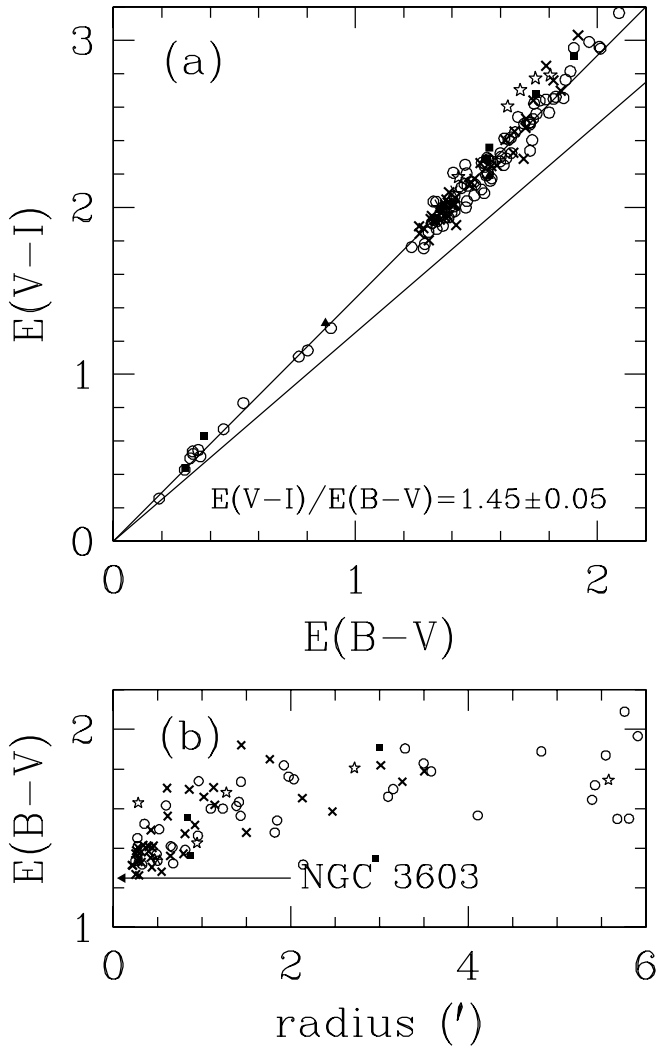

FIG. 5.—Reddening law and $E(B-V)$ variation. (*a*) $E(V-I)$ vs. $E(B-V)$ relation. The lower solid line represents the normal relation, $E(V-I)/E(B-V) = 1.25$, while the upper one denotes the color excess ratio from the early-type ($Q \leq -0.55$) stars in the observed region. (*b*) $E(B-V)$ variation. $E(B-V)$ increases rapidly as the distance from the cluster center increases. All symbols are the same as in Fig. 4.

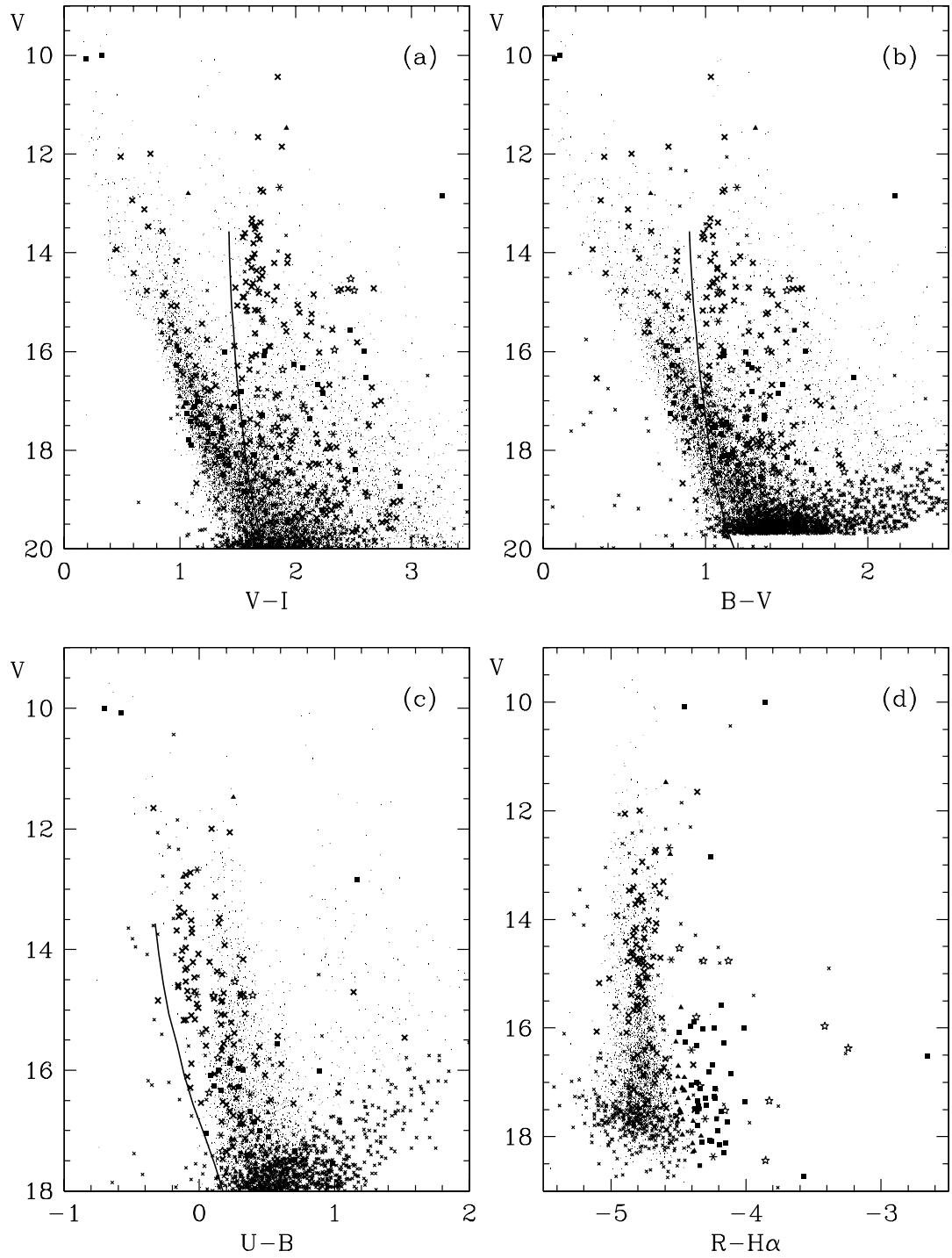

FIG. 6.—Color-magnitude diagrams from SSO observations. The solid line represents the reddened ZAMS relation. All symbols are the same as in Fig. 4.

find the best-fitting ZAMS line to the observed MS stars in Figure 7 (*top right*) and determined a value $E(R-I)/E(B-V) = 0.80$ that is slightly higher than the normal value [for example, $E(R-I)/E(B-V) = 0.74$, Bessell et al. 1998], but it is consistent with the value obtained by Sagar et al. (2001). In the (V, $R-I$) CMD we also plotted the PMS evolutionary track (for 1 $M_{\odot}$; *thick solid line*, *bottom right*, Fig. 7) of Baraffe et al. (1998) (using their original colors). Baraffe et al. (1998) and SDF00 are well matched for $R-I \leq 1.6$ mag but disagree for early stages. In addition, Baraffe et al. (1998) gives far older ages for these stars.

Three WN6-type stars are located well above the brightest point of the theoretical ZAMS. The age of MS and WN6 stars is about 2 Myr but is quite uncertain because the nature and evolutionary status of WN6 stars are still controversial. Apparently, MS stars in NGC 3603 (*top left*, Fig. 7) could not be found at $V \geq 19.5$ mag. If we statistically subtract the field-star contribution using the field-star luminosity function derived at $r \geq 7'$ from the (V, $V-I$) CMD of the PC1 region, there are practically no MS stars fainter than $V \approx 18.5$ mag. The mass of MS stars with $V = 18.5$ mag is about 4 $M_{\odot}$, and its PMS lifetime from SDF00 is about 2 Myr. The mean age of the PMS

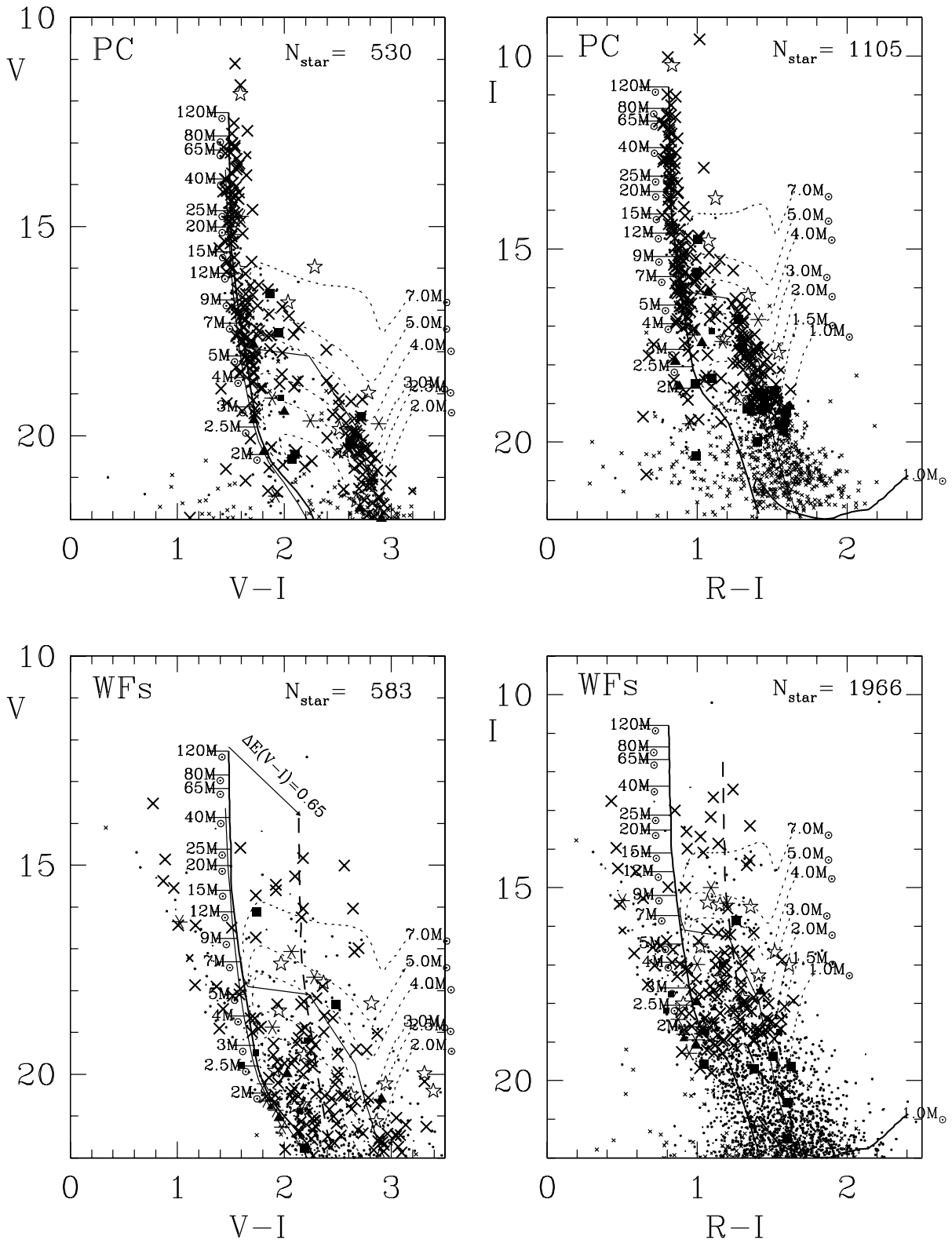

FIG. 7.—Color-magnitude diagrams from *HST* data. The top two panels are CMDs for the stars in the PC1 chip, while the bottom two are those for stars in the WF chips. The thick solid line represents the reddened ZAMS relation from the Geneva models (Schaller et al. 1992), while the dotted lines with mass to the right denote the PMS evolution tracks from Siess et al. (2000). The thin solid line that crosses the PMS locus is the isochrone of age 1 Myr from Siess et al. (2000). The thin solid line just left of the theoretical ZAMS is the empirical ZAMS (Sung and Bessell 1999). In the transformation of physical parameters to observational colors we used the synthetic colors of Bessell et al. (1998). The thick solid line labeled 1.0 $M_{\odot}$ in (I, $R-I$) CMD represents the PMS evolution track of Baraffe et al. (1998). The long dashed line in the bottom panel is the reddened ZAMS relation [reddened by $E(B-V) = 1.70$]. The other symbols are the same as in Fig. 4.

TABLE 4

Hα-Emission Stars and Candidates from SSO Observations

ID	R.A. (J2000.0)	Decl. (J2000.0)	V	$V-I$	$B-V$	$U-B$	$R-$Hα	$\Delta(R-$Hα$)$	Remark[a]
96.....	11 13 29.49	−61 15 51.3	10.082	0.190	0.072	−0.577	−4.454	0.272	Hα, HD 306205 (B0 II)
114.....	11 13 31.41	−61 13 39.5	11.476	1.919	1.309	0.253	−4.593	0.124	Hα C
146.....	11 13 34.73	−61 20 42.6	10.007	0.329	0.103	−0.701	−3.859	0.845	Hα, HD 306209 (B1 Ve)
349.....	11 13 50.75	−61 17 48.8	16.253	1.982	1.265	0.111	−4.448	0.252	Hα
471.....	11 14 01.49	−61 03 48.6	15.570	2.468	1.549	0.576	−4.186	0.553	Hα

Note.—Table 4 is presented in its entirety in the electronic edition of the Astronomical Journal. A portion is shown here for guidance regarding its form and content.

[a] Hα: Hα-emission star; Hα C: Hα-emission candidate; X: X-ray–emission star; SB means the stars from this photometry. The numbering system used is 1–2044: bright stars ($V \leq 17$) from SSO observation; 10001–11117: stars in PC1; 20001–20892: stars in WF2; 30001–30701: stars in WF3; 40001–40746: stars in WF4; and 50001–60772: faint stars ($V > 18$) from SSO observations.

stars in the core region is well fitted to the PMS isochrone of age 1.0 Myr.

For an extremely young open cluster such as NGC 3603, the age estimated from the location of massive stars in the CMDs is very uncertain because the photometric colors available cannot give the effective temperature precisely. In addition, spectral types themselves are uncertain by one to two subclasses, depending on the author. In many cases the turn-on age of PMS stars is larger than the age of other PMS stars at their earlier stage (see § 5.1 of Sung et al. 1997). Considering these points, it is safe to adopt an age of the cluster of 1.0 (±1.0) Myr. The scatter of PMS stars around the 1 Myr isochrone is comparable to that of the bright MS stars. This means that there is no appreciable age spread in the cluster. The age spread conjectured from the scatter is less than 3 Myr. This implies that the star formation in the core is nearly coeval.

The CMDs from the *HST*/WF chips are also presented in the bottom two panels of Figure 7 . The CMD morphology of the stars in the WF chips is far different from that in the PC1 chip. To the left of the reddened ZAMS one can easily find the blue stars in the foreground Sgr-Car arm. But to the right of the ZAMS most X-ray–emission stars (and Hα-emission stars) are simply scattered, and there is no obvious sequence of cluster stars. As mentioned in § 3.1, the reddening increases rapidly at $r \geq 0.'2$ from $E(B-V) \approx 1.25$ mag to ∼1.8 mag, and so we plotted a more reddened ZAMS line [$E(B-V) = 1.70$, i.e., $\Delta E(V-I) = 0.65$] in the bottom two panels of Figure 7 (*dashed line*). The dashed line crosses the mean distribution of X-ray–emission stars, implying that most X-ray–emission stars to the right of the reddened ZAMS (*solid line*) are MS/PMS stars in NGC 3603 or at least young stars associated with the older group of young stars scattered around NGC 3603 (see § 5.1). In addition, the range of reddening in the outer region of NGC 3603 is much larger than that estimated from the bright early-type stars (see § 2.1). The range of reddening $E(B-V)$ is from about 1.25 mag in the center up to ∼2.1 mag in the outer region.

3.3. Hα-Emission Stars

3.3.1. Hα-Emission Stars from SSO Observations

Hα emission is one of most prominent features of T Tauri stars as well as of Herbig Ae/Be stars. Sung et al. (1997) and SBL98 used the Hα-emission index $R-$Hα as a very important membership criterion for low-mass PMS stars in NGC 2264 and NGC 6231. The same technique is applied to the stars in the observed region to select Hα-emission stars.

We assigned the same criteria as in Sung et al. (1997) and SBL98, i.e., $\Delta(R - \text{H}\alpha) \geq 0.2$ for Hα-emission stars and $\Delta(R - \text{H}\alpha) \geq 0.1$ for Hα-emission candidates. From this procedure we selected 73 Hα-emission stars and candidates. These are listed in Table 4. Two known emission-line stars (HD 306205 and HD 306209)[3] are classified as Hα-emission stars from our photometry. SB 1398 is also classified as an Hα-emission star from *HST* images (see § 3.3.2 and Table 5). One of the brightest stars, SB 1266 (= SB 10635, Sp: WN6 + abs) is classified as an Hα-emission star from ground-based observations, but the star is located near the cluster center, and therefore the photometric data for the star may be inaccurate. The star's image is saturated in the Hα observation from the *HST* archive.

The spatial distribution of these stars does not show any definite concentration around the center of NGC 3603. As mentioned in § 3.2, the Hα technique itself could not give any definite information on the PMS membership of NGC 3603.

3.3.2. Hα-Emission Stars from HST Images

Most ground-based data were obtained in poor seeing conditions, and the detection of faint Hα-emission stars is

[3] See http://simbad.u-strasbg.fr.

TABLE 5

Hα-Emission Stars and Candidates from *HST* Observations

ID	R.A. (J2000.0)	Decl. (J2000.0)	V	$V-I$	ΔHα	Remark[a]
1159.....	11 15 03.52	−61 15 45.8	15.746	1.718	−0.205	Hα C+X
1398.....	11 15 13.87	−61 15 58.1	16.327	2.062	−1.095	Hα
10003.....	11 15 04.90	−61 15 45.1	19.103	1.973	−0.293	Hα C
10017.....	11 15 05.15	−61 15 37.3	22.613	3.220	−0.350	Hα
10018.....	11 15 05.16	−61 15 29.7	19.930	2.684	−0.534	Hα+X

Note.—Table 5 is presented in its entirety in the electronic edition of the Astronomical Journal. A portion is shown here for guidance regarding its form and content.

[a] Hα: Hα-emission star; Hα C: Hα-emission candidate; X: X-ray–emission star.

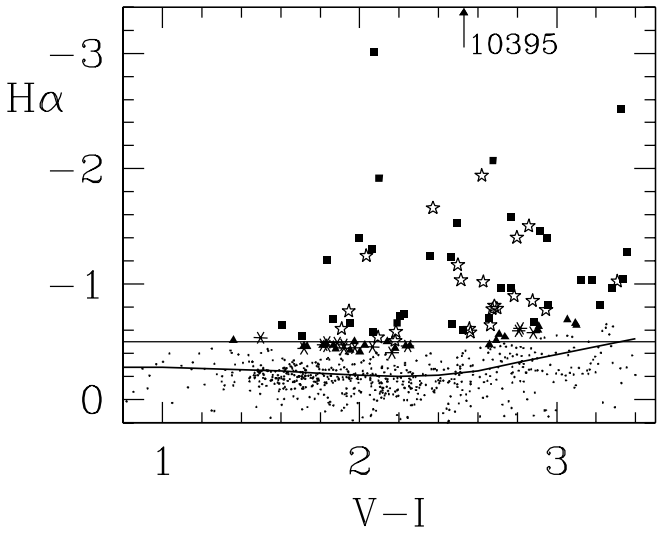

FIG. 8.—Identification of Hα-emission stars from the *HST* images. To identify Hα-emission stars we used the pseudo-continuum magnitude $(V+I)/2$ as the continuum reference level at Hα (Sung et al. 2000). The thin line represents the lowest level of Hα-emission stars used in Sung et al. (2000), while the thick line denotes the mean Hα index [$\equiv m_{\rm H\alpha} - (V+I)/2$] for non-Hα-emission stars. We tentatively assigned stars with ΔHα index ≤ -0.3 as Hα-emission stars and those with Δ Hα index ≤ -0.2 as Hα-emission candidates. The other symbols are the same as in Fig. 4.

therefore very limited as a result of the bright, spatially varying nebula. However, *HST* images are nearly diffraction-limited images and so are very useful to detect the faint Hα-emission stars. We have already shown its usefulness in Sung et al. (2000). To detect faint Hα-emission stars, we retrieved and used *HST* images observed in the nebular filters (Hα: F656N; [N II]: F658N).

We present the Hα index [$\equiv m_{\rm H\alpha} - (V+I)/2$] versus $V-I$ diagram in Figure 8. The mean magnitude of V and I was used as a pseudocontinuum magnitude at Hα as in Sung et al. (2000). Because in the Lagoon nebula the number of measured stars was very small, it was very difficult to derive the mean relation for stars without Hα emission. But in NGC 3603 it is now possible to draw the mean relation between $V-I$ and the Hα index for stars without Hα emission. The thick line in Figure 8 is the adopted relation. Many stars without Hα emission in the Lagoon nebula have an Hα index of around 0 (see Fig. 7 of Sung et al. 2000), but in NGC 3603 many stars are shifted toward negative values. This might be related to the difference in reddening.

We assigned stars with ΔHα index [$\equiv$ Hα(star) − Hα (meanline)] ≤ -0.3 as Hα-emission stars and with ΔHα ≤ -0.2 as Hα-emission candidates. This criterion is very similar to that of Sung et al. (2000) for $(V-I) \leq 2.5$, but it is slightly more stringent for redder stars. Using this procedure, we selected 96 Hα-emission stars from *HST* images. These are listed in Table 5. Most faint blue Hα-emission stars ($V \geq 19$ mag) with $(V-I) \leq 2.4$ seem to be foreground young stars (see § 3.2 for the discussion of faintest MS star in NGC 3603).

3.4. *Distance of NGC 3603*

Sher (1965) determined the first distance of $d = 3.5$ kpc. Later, Mo74 obtained a much larger value ($d = 8.1 \pm 0.8$ kpc). Van den Bergh (1978) derived $d \sim 7$ kpc for the cluster, which is consistent with the kinematic distance. The currently accepted distance to the cluster is 7 ± 1 kpc.

To derive the distance to the cluster, we have drawn two diagrams in Figure 9. We introduced a new reddening-free index Q_{VI} [$\equiv V-2.45(V-I)$]. Q_{VI} is simply taken from the relation $R_V \equiv A_V/E(B-V) = 2.45E(V-I)/E(B-V)$ (Guetter & Vrba 1989). The usefulness of Q_{VI} is not yet widely known. But the use of the index is probably limited because of the somewhat larger scatter in $V-I$ among early-type stars (see Fig. A1 of Sung & Bessell 1999). Admitting such a limitation, we have drawn the (Q_{VI}, Q) diagram in Figure 9*a*. Ten less reddened early-type stars (*large dots*) are well matched to the ZAMS line of $V_0 - M_V \approx 11.0$ mag ($d \approx 1.6$ kpc). But the other more reddened early-type stars are distributed vertically. Apparently, the lower boundary of these stars is matched to the ZAMS line of $V_0 - M_V \approx 14.2$ mag ($d \approx 6.9$ kpc). Because of the lack of reliable $U-B$ data for faint stars it is very difficult to determine the distance accurately.

The other way to determine the distance to NGC 3603 is to use the observed (V, $V-I$) CMD for the central region. With the known reddening law for the region (see § 3.1) and the distance modulus obtained above we have drawn a reddened

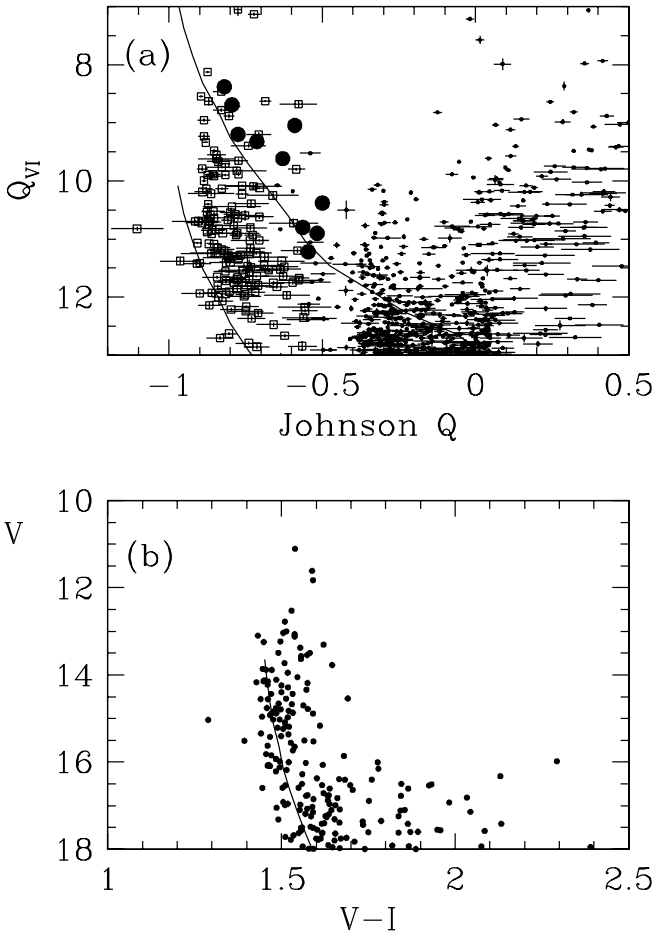

FIG. 9.—(*a*) Q_{VI} [$\equiv V-2.45(V-I)$] vs. Johnson Q diagram for $V \leq 17$ mag and $r \geq 0\farcm3$. Large dots, open squares, and small dots represent, respectively, less reddened early-type stars ($U-B \leq -0.1$, $B-V \leq 0.3$, and $Q \leq -0.50$), more reddened early-type stars ($B-V > 0.8$, $U-B \leq 0.9$, and $Q \leq -0.55$), and redder stars. The thin line and thick line represent the ZAMS relation of $V_0-M_V = 11.0$ and 14.2 mag, respectively. (*b*) V vs. $V-I$ diagram for the stars within $r = 0\farcm3$. The solid line represents the reddened ZAMS relation [$V_0-M_V = 14.2$ and $E(B-V) = 1.25$].

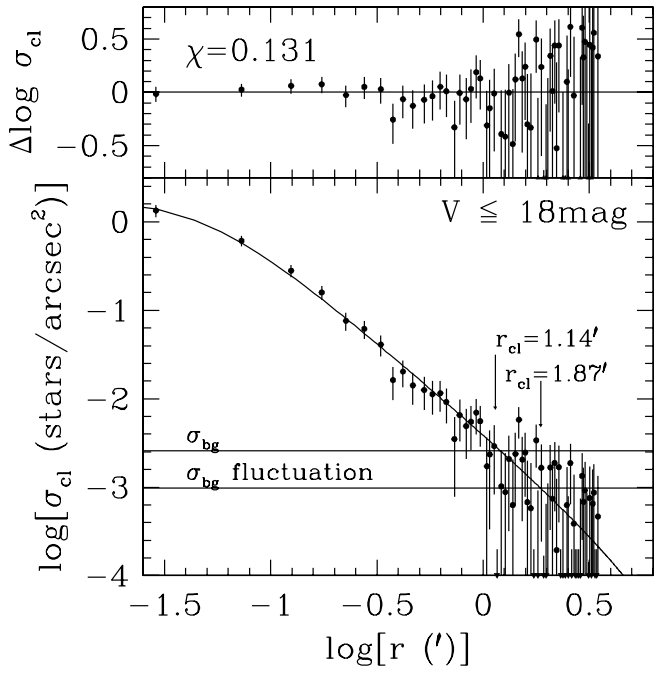

FIG. 10.—Surface density profile of NGC 3603 for $V \leq 18$ mag. The bottom panel shows the radial density profile from the cluster center ($\alpha_{J2000.0} = 11^h15^m7^s.26$, $\delta_{J2000.0} = -61°15'37''.9$—the center of mass of stars with $V \leq 16$ mag). The thin curved line represents the best fit to the empirical King model (King 1962) of $k = 1.91$ arcsec^{-2}, $r_c = 2''.91$, and $r_t = 874''$. The bottom two lines represent, respectively, the surface density of the background ($r \geq 2'.5$) and the fluctuation in the background. The value $r_{cl} = 1'.14$ is the radius where the model surface density reaches 3 times the background fluctuation, while $r_{cl} = 1'.87$ is the radius where the model density reaches the background fluctuation. The top panel shows the goodness of the model fit. The value of χ denotes the reduced χ [$\equiv (\chi^2/\mathrm{dof})^{1/2}$].

ZAMS line on the observed CMD in Figure 9. However, due to the lack of quality $U-B$ data for the stars in the cluster core, it is impossible to determine $E(B-V)$ for individual stars, and in addition, most massive stars may be in a more evolved stage and so may be brighter in V than a ZAMS star. In this respect the distance modulus obtained above is well matched to the cluster sequence. From our limited data it is safe to adopt the distance modulus for NGC 3603 as 14.2 ± 0.2 mag ($d = 6.9 \pm 0.6$ kpc).

3.5. *Radius of NGC 3603*

The radius of a cluster can be determined from the surface-density profile. Sung et al. (1999) determined the radius of the open cluster M11 from the surface-density profile of stars in the MS band. For M11 it is possible to derive the radius because the region around M11 is very transparent and nearly free from differential reddening. But the situation for NGC 3603 is far different because of the irregular distribution of reddening material. Given this limitation, we have tried to determine the radius of NGC 3603 using the radial variation of relatively bright stars ($V \leq 18$ mag). Figure 10 shows the radial variation of the surface density from the cluster center ($\alpha_{J2000.0} = 11^h15^m7^s.26$, $\delta_{J2000.0} = -61°15'37''.9$), that is, the center of mass of stars with $V \leq 16$ mag. In estimating the mass of a star we used the ML relation from Schaller et al. (1992) for age 1 Myr.

We also attempted to fit the observed profile to a King empirical density profile for a spherical system,

$$f(r) = k\left[1/\sqrt{1+(r/r_c)^2} - 1/\sqrt{1+(r_t/r_c)^2}\right]^2$$

(King 1962). The best-fitting parameters are $k = 1.91$ arcsec^{-2}, $r_c = 2''.91$, and $r_t = 874''$. The King profile is very sensitive to the variation in r_c (core radius) and k (the central density) but insensitive to r_t, which is less meaningful for the open clusters in the Galactic plane. In the figure we have marked the surface density of the background region ($r > 2'.5$; see NPG02) and the fluctuation of the background. The estimated radius of NGC 3603 from the optical star count is between $1'.14$ (model density reaches 3 times the background fluctuation) and $1'.87$ (model density reaches the level of the background fluctuation). As mentioned in § 3.1, at $r \geq 0'.3$ the reddening changes abruptly, and therefore a radius that is smaller than that obtained by NPG02 could be a lower limit.

To derive the radius more reliably, we plotted the surface-density variation of X-ray sources in Figure 11. The usefulness of X-ray source counts is that X-rays are less affected by interstellar reddening than the near-IR. We only counted X-ray sources whose significance is greater than 5. The surface density of detected X-ray sources (*filled circles*) decreases monotonically from the center. But the detection probability also decreases as the distance from the aim point, which is very close to the cluster center. The detection probability at a given significance level is the product of the effective area of the High Resolution Mirror Assembly (HRMA) of the *Chandra X-Ray Observatory* and the peak value of the source. We assume that the PSF of an X-ray source follows a Gaussian profile and its FWHM is the radius of the circle enclosing 85% of the power. All this information is available from the *Chandra* Proposers' Observatory Guide[4] or CIAO.[5] After correcting for the detection probability, the radial profile of the

[4] At http://asc.harvard.edu/proposer.

[5] The *Chandra* Interactive Analysis of Observations, at http://asc.harvard.edu/ciao.

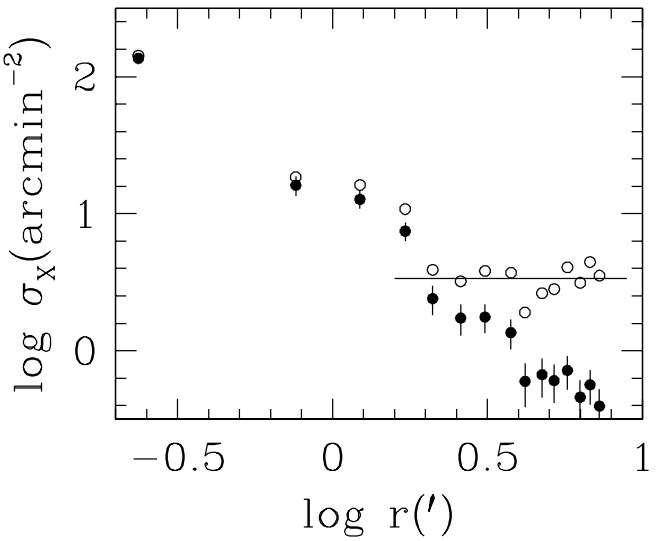

FIG. 11.—Surface density profile of X-ray sources. The filled circles and open circles represent the detected surface density of X-ray sources and the surface density of X-ray sources corrected for detection probability (see the text for more details). The line in the figure indicates the mean surface density at $r \geq 2'.5$.

X-ray source density is changed mainly at large r. For $r \geq 2'$, the surface density no longer falls off.

At this point we can strongly say that the radius of NGC 3603 is about $2'$, which is larger than that derived from optical star counts, but smaller than that determined from near-IR star counts by NPG02. We believe that the NPG02 value can be questioned. As mentioned above, King profile fitting is very sensitive to the central density as well as the core radius. Our optical photometry based on *HST* images gives a better star content at the very center of NGC 3603, whereas the radius determined by NPG02 based on ground-based near-IR photometry is strongly affected by saturation of the bright stars in the cluster center. Therefore, the central density k from their model fit could be underestimated.

4. INITIAL MASS FUNCTION

4.1. *Completeness Test*

Completeness of photometric data is of crucial importance in the study of the luminosity and mass functions. The main factor affecting the completeness of data is crowding. Most ground-based data for globular clusters and even relatively dense open clusters like M11 (Sung et al. 1999) are strongly affected by the effects of crowding. On the other hand, data for relatively sparse open clusters can also be incomplete because of the hiding of faint stars in the bright wings of saturated images (Sung & Bessell 1999). Sung et al. (1999) performed a Monte Carlo simulation of a model cluster having a similar density profile and estimated the completeness of the photometry.

The situation for NGC 3603 is very similar to that of M11, even though the central region has been observed by *HST*. Although the spatial resolution of *HST* images is far superior to that obtained with ground-based telescopes, the bright wings and spikes strongly affect the finding and measurement of faint stars, especially in the center of NGC 3603, as a result of the dense clustering of bright stars. First we tried to use the completeness test option or "fake_image" routine in HSTPHOT (Dolphin 2000). But the HSTPHOT routine uses only the central 13×13 pixels of the Tiny Tim model PSF. The profile of this stellar PSF is far from reproducing the effect of bright wings or spikes on the completeness.

To estimate the completeness properly, we tried to model a cluster having a similar density profile and luminosity function using a Monte Carlo method. To simulate it more realistically, we subtracted all stars in the shortest exposure images and then added and multiplied constants to the subtracted images so that the level of the background brightness and its fluctuation was similar to those of the original images. Next we added about 1400–2000 stars down to $V \approx 24$ mag to each image using the ADDSTAR task in IRAF/DAOPHOT with the empirical PSF derived for up to $r = 17$ pixels from relatively bright, isolated stars. Finally, we ran HSTPHOT as well as DAOPHOT and checked by eye whether a star was real or a spurious detection of a wing or a spike. The visual inspection was very important for faint stars. For example, the number of spurious detection from HSTPHOT was more than 2500, but that from IRAF/DAOPHOT with the added visual inspection was only about 30.

Although we did many model simulations, the last two were the most successful. We will only discuss the results from these two simulations (cl6 and cl7). The input and output CMDs of cl7 at three different regions are compared in Figure 12. For the outer region, the output CMD is nearly identical to the input one. But for the inner region the output CMD shows somewhat larger scatter due to the increase in photometric errors. If we define the completeness as the simple finding of stars, the overall completeness is quite good, e.g., better than or similar to 90% down to $V = 22$ mag. But for the inner region ($r \leq 0.''1$) the completeness reached about 90% at $V = 18.5$, while for the outer region ($r > 0.''2$) the completeness was better than 90% down to $V \approx 23.5$ mag.

Researchers generally try to isolate the locus of member stars to minimize the contamination of field stars. In this respect much attention should be paid to the estimation of completeness. Because of the effect of crowding photometric errors increase, and therefore the widths of the MS or PMS bands become wider. If stars measured are distributed evenly in the CMDs, the number of stars in a given locus will be conserved. Because the locus of members is a relatively dense part of the CMDs, the actual number of member stars will decrease as a result of the increase in photometric errors. We divided the CMD into three groups: MS stars, PMS stars, and field stars, then calculated the completeness for each group. Since few MS stars fainter than $V = 18.5$ mag could be found, we merged the two groups (MS and PMS) into one. Even though the effect of crowding is very severe in the central region ($r \leq 0.''1$), the completeness is better than 90% for $V \leq 18$ mag. At fainter magnitudes the completeness drops rapidly.

4.2. *The IMF of the Core of NGC 3603*

The masses of individual stars were determined by using the theoretical ML relation from the Geneva models (Schaller et al. 1992) for MS stars and SDF00 for PMS stars of age 1 Myr. The number of stars in a logarithmic mass interval of $\Delta \log m = 0.2$ were counted. Although Massey & Vukovich (2002) obtained 57 $M_\odot$ for the mass of the O3 V (+O6 V) binary in the R136 cluster, we assumed the upper limit of the most massive stars to be 100 $M_\odot$ because the nature and evolutionary status of WN6 are still controversial. There are four known O3 V stars in the center of NGC 3603 (Drissen et al. 1995), and the average mass of these stars using the theoretical ML relation is 52 ± 15 $M_\odot$ ($V = 12.54 \sim 13.58$). The average mass of these stars is slightly smaller than, but consistent with the mass of O3 V stars obtained by Massey & Vukovich (2002).

In § 3.5 we determined the radius of NGC 3603. But because of the irregular distribution of interstellar reddening material and a lack of reliable $U-B$ data for faint stars in the halo region of the cluster, we decided to derive the IMF of the core region (i.e., *HST*/PC1 region) only. The incompleteness of data for fainter stars was corrected for, but the effect of differential reddening was not taken into account. In statistical terms we were able to estimate the contribution of the field stars from the luminosity function of field stars derived from $r \geq 7'$. The estimated number of field stars contaminating the *HST*/PC1 region is about 8.2 stars. But if we limit our attention to the MS ($V = 11 \sim 18.5$ mag) and PMS ($V = 16 \sim 20$ mag) loci only, the number reduces to 1.3 stars, which is negligible.

To investigate the radial variation of the IMF slope, we divided the *HST*/PC1 region into three ($r \leq 0.''1$, $r = 0.''1$–$0.''2$, and $r > 0.''2$). The derived IMFs and IMF slopes are presented in Figure 13. The slope of the IMF calculated for $\log m \geq 0.4$ is noted in the figure. In the figure we could not find a definite turnover or truncation in the IMF. Even in the core itself the IMF increases as the mass decreases down to the limit of the observations. The slope of the IMF in the core is very flat

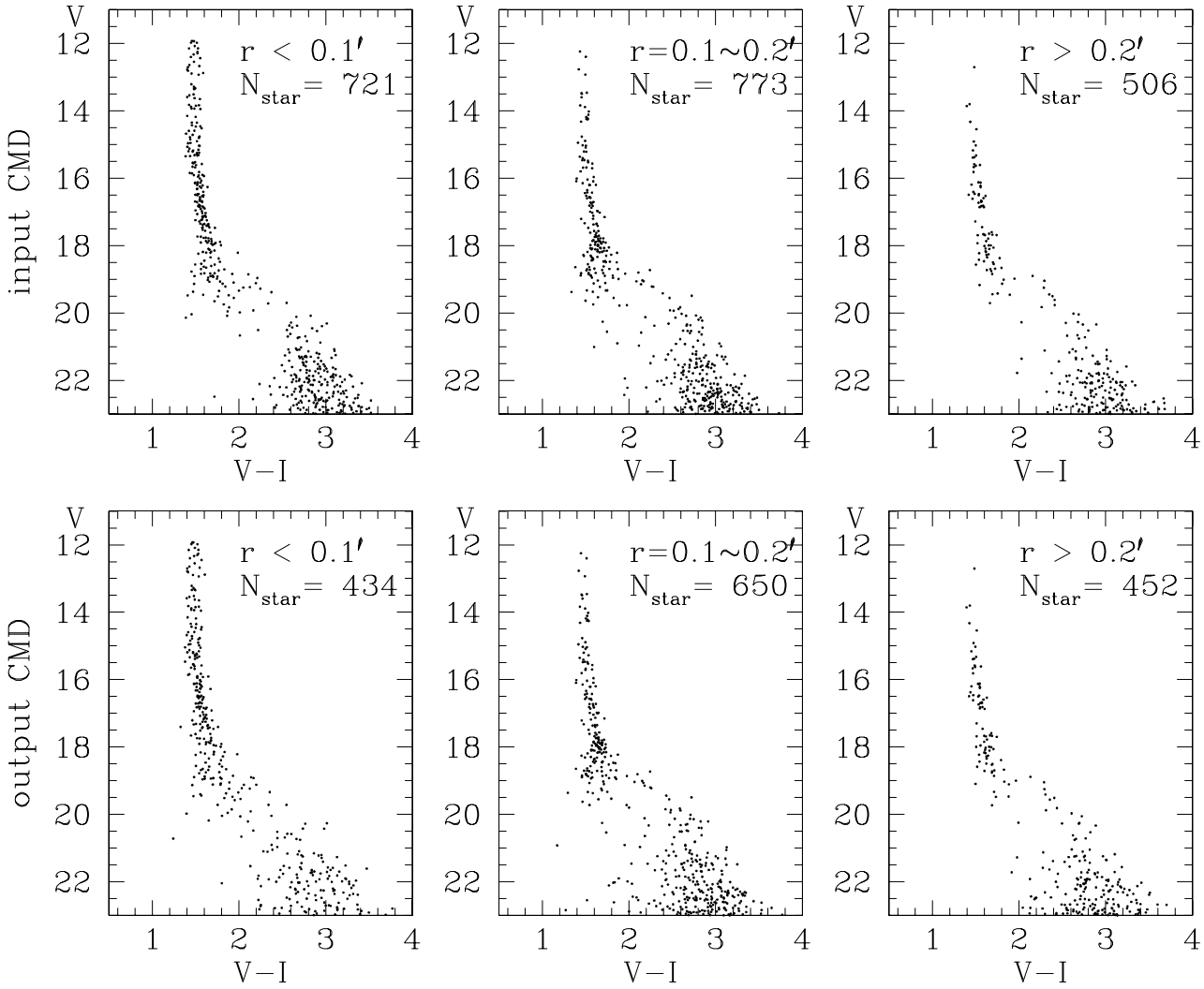

FIG. 12.—Input and output CMDs of model cluster cl7. The top three panels show the input CMDs for three different regions, while the bottom three panels show the output CMDs.

$\Gamma[\equiv d\log \xi(\log m)/d \log m] = -0.5 \pm 0.1$. In addition, the surface density of stars is incredibly high, e.g., about 1250 times higher than that of NGC 6231 (SBL98) at $\log m = 1.5$. The slope of the IMF changes systematically. It becomes steeper as the distance from the center increases. At $r > 0.''2$ it is similar to that of NGC 6231 ($\Gamma = -1.2 \pm 0.4$, SBL98), but its surface density is still very high—about 50 times higher than that of NGC 6231 at $\log m = 1.5$.

The IMF of the whole *HST*/PC1 region (*filled circles*) was also calculated and presented in the figure. It shows a steepening at $\log m \geq 1.6$ ($\Gamma = -1.8 \pm 0.1$) and a weak signature of a flattening between $\log m = 1.0$–1.5. Hofmann et al. (1995) obtained the slope of the IMF using 28 stars in the central $\sim 6.''3 \times 6.''3$ region. Their value was $\Gamma = -1.59$, but from our data the IMF slope for central region ($r \leq 0.''1$, $\log m \geq 1.3$) is -0.95 ± 0.10, which is much flatter. Such a difference may be caused by the ML relation used. On the other hand, Eisenhauer et al. (1998) obtained $\Gamma = -0.73$ from near-IR photometry, which is slightly flatter than that obtained for the whole *HST*/PC1 region. They subtracted the field-star contribution obtained at $r \geq 50''$. Their flat IMF could probably be caused by an oversubtraction of field-star contamination, because in the outer regions the low-mass stars are dominating, as can be inferred from the change in the IMF slopes as well as the deficit of massive stars at $r > 0.''2$.

5. DISCUSSION

5.1. *The Star Formation History in NGC 3603*

The Hertzsprung-Russell (H-R) diagram serves as the most important diagnostic tool for studying a stellar system. To understand the star formation history and stellar content in NGC 3603, we constructed the H-R diagram of early-type stars ($Q \leq -0.55$) in the halo of NGC 3603 ($r = 0.''3 \sim 2'$) in Figure 14. We selected 71 early-type stars from the SSO data and transformed their magnitudes and colors to physical parameters using the calibrations described in SBL98. The stellar evolution models of Schaller et al. (1992) are superposed. The theoretical ZAMS and an isochrone of age 5 Myr are also overlaid on the figure.

Actually, the isochrone for age 5 Myr interpolated from these evolution models has little meaning, because the evolutionary tracks of a 40 $M_\odot$ star and 25 $M_\odot$ star are very different. But as the highly evolved blue supergiant Sher 25 (B1.5Iab) is known to have evolved from a red supergiant (Brandner et al. 1997), its evolutionary track should be very

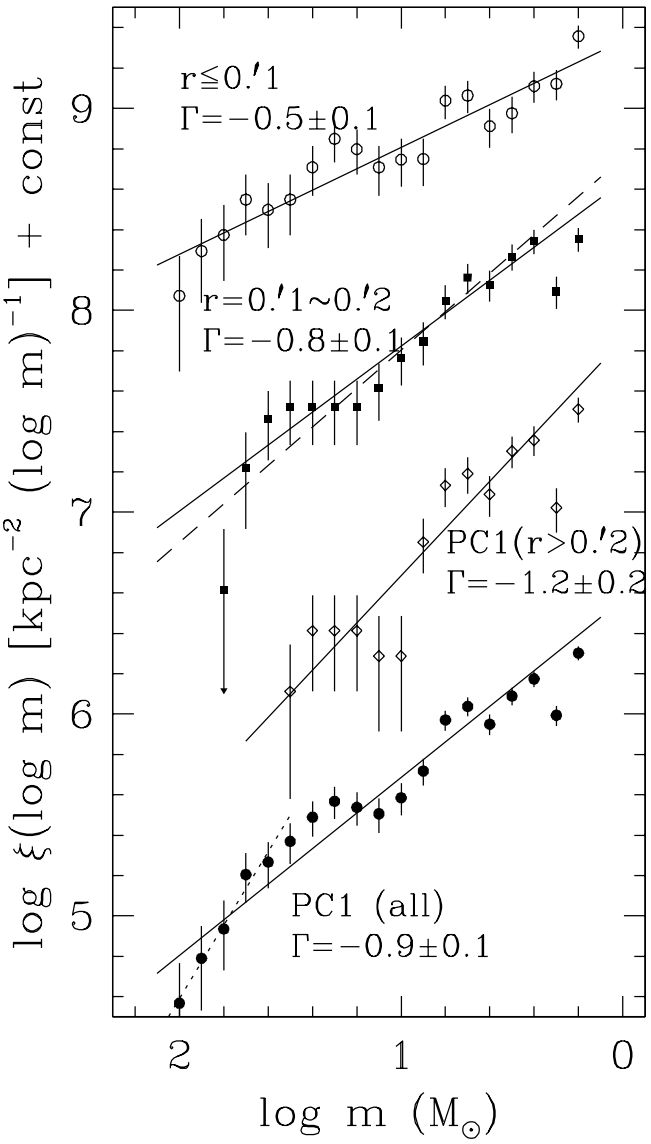

FIG. 13.—IMF of the core of NGC 3603. The IMF corrected for data completeness is estimated and shown for three different regions and the whole region of the *HST*/PC1 chip using the theoretical ML relation from the Geneva models (Schaller et al. 1992) and Siess et al. (2000) for age 1 Myr. In the calculation we used the mass interval $\Delta \log m = 0.2$ to enlarge the number of stars for given mass bin. To reduce the binning effect, we also calculated the IMF in the same mass bin but shifted by 0.1 in $\log m$. To show the radial variation of the IMF clearly, we have shifted the IMF vertically by 0, −0.5, −1.0, and −2.5 in logarithmic scale from top to bottom. The slope of the IMF Γ is estimated for $\log m \geq 0.4$. For $r = 0.'1 \sim 0.'2$, we neglected the most massive mass bin (containing only one star) in calculating the IMF slope. If we include the highest mass bin, the slope of the IMF becomes somewhat steeper, with a value of $\Gamma = -0.95 \pm 0.1$ (*dashed line*). The dotted line in the bottom graph shows a fairly steep IMF for the most massive stars ($\Gamma = -1.8 \pm 0.1$ for $\log m \geq 1.6$).

similar to that of a 40 $M_\odot$ star. The detailed evolutionary status of another blue supergiant Sher 23 (O9.5Iab) is not as well known. Apparently, its age is slightly younger (about 3.7 Myr) than Sher 25 because no peculiarity in its spectrum has been reported. Three of the mid–O-type stars [Sher 18-O6 If, Sher 47-O4 V, and Sher 22-O5 V(f)] are even younger than the others. Their ages (about 1.8 Myr) are very similar to that of stars in the core, and they therefore may have the same star formation history. NPG02 found an enhancement of stars in the southeast-east direction. These three mid–O-type stars are located in the east or southeast of NGC 3603's core, while the two blue supergiants are located in the north or northeast region. The slight differences in age and their different locations suggests that they might have a different star formation history. The age difference between Sher 25 and the other early-type stars in the halo and NGC 3603 core is about 3 Myr, which is the lifetime of the most massive star. This result supports the suggestion by Melnick et al. (1989) that sequential star formation has propagated from north to south (see also De Pree, Nysewander, & Goss 1999). Sequential star formation is also supported by the existence of large-scale gas motions around NGC 3603, which was probably set up by the action of earlier supernovae (Clayton 1986).

In the H-R diagram many bright early-type stars ($M_{\rm bol} = -7.5 \sim -9$, $\log T_{\rm eff} \approx 4.48$) are distributed vertically. Their effective temperatures were estimated from $(U-B)_0$. As mentioned by Massey (1985), *UBV* colors are degenerate for very hot stars, and spectral types are better used as temperature indicators for O-type stars. However, no spectral type are available for these stars and therefore it is very difficult to properly locate them on the H-R diagram. Among the underluminous early-type stars ($M_{\rm bol} = -4 \sim -7.5$), stars in the south of NGC 3603 are marginally younger than those in the north. To investigate the star formation history in NGC 3603, spectral classification or far-UV colors of these stars are required.

Using the limited number of stars in the halo, we have calculated the IMF and find that the IMF is fairly steep. The slope of the IMF for $\log m \geq 1.2$ is -1.9 ± 0.4. This value is very similar to the IMF of the massive stars in NGC 3603's core (see the last paragraph of § 4.2).

6. SUMMARY

We have performed *UBVRI* and Hα photometry of the starburst cluster NGC 3603. In the present study we used ground-based images as well as archival data from the *HST* and the *Chandra X-Ray Observatory*. We presented the CMDs of the cluster core. In the CMDs of the stars in the *HST*/PC1, well-defined MS and low-mass PMS stars can clearly be seen.

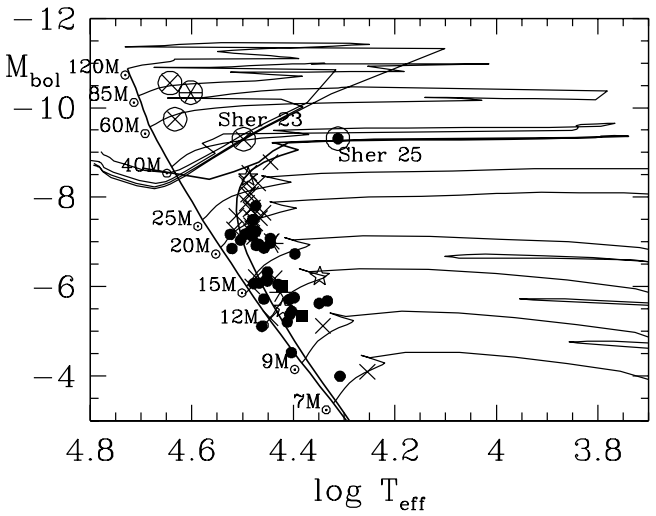

FIG. 14.—H-R diagram for early-type stars in the halo region of NGC 3603 ($r \leq 2'$). The thick solid lines represent the theoretical ZAMS and isochrone of age 5 Myr. The thin solid lines with mass to the left are the stellar evolution models of Schaller et al. (1992). Symbols surrounded with a circle denote stars with known spectral type. Other symbols are the same as in Fig. 4. The two evolved supergiants (Sher 23 and 25) are marked.

NGC 3603 contains the most massive stars (possibly more massive than 100 $M_{\odot}$), as well as very low-mass PMS stars. Using the stellar evolution models by the Geneva group and PMS evolution tracks by SDF00, we determined the age of the cluster to be 1 ± 1 Myr. From the scatter of PMS stars, the age spread in the core is less than 3 Myr, i.e., the star formation in NGC 3603 is nearly coeval. We also performed a completeness test by employing a Monte Carlo method to obtain the fraction of stars missed because of the bright wings or spikes in the stellar PSF of *HST* images. The incompleteness is severe in the *HST* observations of the very dense core of NGC 3603 as a result of the presence of many bright saturated stars. For $r \geq 0\farcs2$ the incompleteness is not as severe.

Using the theoretical ML relation, we derived the IMF of the cluster. The surface density of the core is enormously high. The slope of the IMF is very flat ($\Gamma = -0.5 \pm 0.1$) and shows a gradual steepening ($\Gamma = -0.8 \pm 0.1$ at $r = 0\farcs1 \sim 0\farcs2$; $\Gamma = -1.2 \pm 0.2$ at $r > 0\farcs2$ of *HST*/PC1). The slope in the IMF from the whole *HST*/PC1 region is moderately flat, $\Gamma = -0.9 \pm 0.1$. The IMF in the outer region could not derived because of the rapid variation in interstellar reddening, as well as a lack of reliable $U-B$ data for faint stars.

Using a measure of Hα emission, the $R-$Hα color from SSO data or the Hα index for *HST* data, we selected Hα-emission stars or Hα-emission candidates. Many Hα-emission stars were found to be spread over the observed region and therefore are probably young stars in the general field of the Sgr-Car arm. By introducing a reddening-free parameter Q_{VI}, we derived the distance modulus of NGC 3603 ($V_0 - M_V = 14.2 \pm 0.2$, i.e., $d = 6.9 \pm 0.6$ kpc). Using the surface-density profile of stars as well as X-ray sources, we determined the radius of NGC 3603 to be $r_{\rm cl} \approx 2'$, which is slightly smaller than that determined from near-IR star counts in NPG02. Using the H-R diagram for a very limited group of early-type stars in the halo region, some discussion was offered on the star formation history in NGC 3603.

H. S. acknowledges the support of the Korea Science and Engineering Foundation to the Astrophysical Research Center for the Structure and Evolution of the Cosmos at Sejong University. The authors would like to thank the anonymous referee for many useful suggestions.

REFERENCES

Balick, B., Boeshaar, G. O., & Gull, T. R. 1980, ApJ, 242, 584
Baraffe, I., Chabrier, G., Allard, F., & Hauschildt, P. H. 1998, A&A, 337, 403
Bessell, M. S., Castelli, F., & Plez, B. 1998, A&A, 333, 231
Brandl, B., Brandner, W., Eisenhauer, F., Moffat, A. F. J., Palla, F., & Zinnecker, H. 1999, A&A, 352, L69
Brandner, W., Grebel, E. K., Chu, Y.-H., & Weis, K. 1997, ApJ, 475, L45
Brandner, W., et al. 2000, AJ, 119, 292
Clayton, C. A. 1986, MNRAS, 219, 895
De Pree, C. G., Nysewander, M. C., & Goss, W. M. 1999, AJ, 117, 2902
Damiani, F., Maggio, A., Micela, G., & Sciortino, S. 1997, ApJ, 483, 350
Dolphin, A. E. 2000, PASP, 112, 1383
Drissen, L., Moffat, A. F. J., Walborn, N. R., & Shara, M. M. 1995, AJ, 110, 2235
Eisenhauer, F., Quirrenbach, A., H. Zinnecker, H., & Genzel, R. 1998, ApJ, 498, 278
Frogel, J. A., Persson, S. E., & Aaronson, M. 1977, ApJ, 213, 723
Guetter, H. H., & Vrba, F. J. 1989, AJ, 98, 611
Hofmann, K.-H., Seggewiss, W., & Weigelt, G. 1995, A&A, 300, 403
Holtzman, J. A., Burrows, C. J., Casertano, S., Hester, J. J., Trauger, J. T., Watson, A. M., & Worthey, G. 1995, PASP, 107, 1065
King, I. 1962, AJ, 67, 471
Massey, P. 1985, PASP, 97, 5
Massey, P., & Vukovich, J. 2002, ApJ, 565, 982
Melnick, J., & Grosbøl, P. 1982, A&A, 107, 23
Melnick, J., Tapia, M., & Terlevich, R. 1989, A&A, 213, 89
Moffat, A. F. J. 1974, A&A, 35, 315 (Mo74)
———. 1983, A&A, 124, 273
Moffat, A. F. J., Drissen, L., & Shara, M. M. 1994, ApJ, 436, 183
Moffat, A. F. J., et al. 2002, ApJ, 573, 191
Nürnberger, D. E. A. 2003, A&A, 404, 255
Nürnberger, D. E. A., & Petr-Gotzens, M. G. 2002, A&A, 382, 537 (NPG02)
Nürnberger, D. E. A., & Stanke, T. 2003, A&A, 400, 223
Pandy, A. K., Ogura, K., & Sekiguchi, K. 2000, PASJ, 52, 847
Sagar, R., Munari, U., & de Boer, K. S. 2001, MNRAS, 327, 23
Schaller, G., Schaerer, D., Meynet, A., & Maeder, A. 1992, A&AS, 96, 269
Siess, L., Dufour, E., & Forestini, M. 2000, A&A, 358, 593 (SDF00)
Sher, D. 1965, MNRAS, 129, 237
Stetson, P. 1990, PASP, 102, 932
Sung, H., & Bessell, M. S. 1999, MNRAS, 306, 361
———. 2000, Publ. Astron. Soc. Australia, 17, 244
Sung, H., Bessell, M. S., & Lee, S.-W. 1997, AJ, 114, 2644
———. 1998, AJ, 115, 734 (SBL98)
Sung, H., Bessell, M. S., Lee, H.-W., Kang, Y. H., & Lee, S.-W. 1999, MNRAS, 310, 982
Sung, H., Chun, M.-Y., & Bessell, M. S. 2000, AJ, 120, 333
van den Bergh, S. 1978, A&A, 63, 275
van den Bos, W. H. 1928, Bull. Astron. Inst. Netherlands, 4, 261
Walborn, N. R. 1973, ApJ, 182, L21